

Article

X-ray and Nuclear Spectroscopies to Reveal the Element-Specific Oxidation States and Electronic Spin States for Nanoparticulated Manganese Cyanidoferrates and Analogs

Hongxin Wang^{1,*}, Songping D. Huang^{2,*}, Anthony T. Young³, Stephen P. Cramer¹, Yoshitaka Yoda⁴ and Lei Li^{5,†}¹ SETI Institute, Mountain View, CA 94043, USA; spjcramer@mac.com² Department of Chemistry and Biochemistry, Kent State University, Kent, OH 44242, USA³ Lawrence Berkeley National Laboratory, Berkeley, CA 94720, USA; atyoungcal@gmail.com⁴ Precision Spectroscopy Division, SPring-8 Facility, Japan Synchrotron Radiation Research Institute (JASRI), Sayo 679-5198, Japan; yoda@spring8.or.jp⁵ Synchrotron Radiation Research Center, Hyogo Science and Technology Association, Kouto 679-5165, Japan; lil@mail.iasf.ac.cn

* Correspondence: hongxin.ucd@gmail.com (H.W.); shuang1@kent.edu (S.D.H.)

† Current address: Institute of Advanced Science Facilities, Shenzhen 518055, China.

Abstract: In this publication, the potential non-gadolinium magnetic resonant imaging agent—nanoparticulate $K_2Mn[Fe(CN)_6]$ —its comparison sample $KFe[Co(CN)_6]$, as well as their reference samples were measured and analyzed using Mn, Co and Fe L-edge X-ray absorption spectroscopy (L XAS). From the information obtained, we conclude that $K_2Mn[Fe(CN)_6]$ has a high spin (hs)-Mn(II) and a low spin (ls)-Fe(II), while $KFe[Co(CN)_6]$ has an hs-Fe(II) and an ls-Co(III). In these Prussian blue (PB) analog structures, the L XAS analysis also led to the conclusion that the hs-Mn(II) in $K_2Mn[Fe(CN)_6]$ or the hs-Fe(II) in $KFe[Co(CN)_6]$ bonds to the N in the $[M(CN)_6]^{4-/-3-}$ ions (where $M = Fe(II)$ or $Co(III)$), while the ls-Fe(II) in $K_2Mn[Fe(CN)_6]$ or the ls-Co(III) in $KFe[Co(CN)_6]$ bonds to the C in the $[M(CN)_6]^{4-/-3-}$ ion, suggesting the complexed metalloligand $[Mn(II)$ or $Fe(II)]$ occupies the N-bound site in PB. Then, nuclear resonant vibrational spectroscopy (NRVS) was used to confirm the results from the L XAS measurements: the Mn(II), Eu(III), Gd(III), Fe(II) cations complexed by $[M(CN)_6]^{n-}$ -metalloligand all take the N-bound site in PB-like structures. Our NRVS studies also prove that iron in the $K_2Mn[Fe(CN)_6]$ compound has a 2+ oxidation state and is surrounded by the C donor atoms in the $[M(CN)_6]^{n-}$ ions.

Keywords: nanoparticulate manganese cyanoferrates; non-gadolinium magnetic resonant imaging agents; L-edge X-ray absorption spectroscopy; L XAS; nuclear resonant vibrational spectroscopy; NRVS; oxidation states; electronic spin states



Citation: Wang, H.; Huang, S.D.; Young, A.T.; Cramer, S.P.; Yoda, Y.; Li, L. X-ray and Nuclear Spectroscopies to Reveal the Element-Specific Oxidation States and Electronic Spin States for Nanoparticulated Manganese Cyanidoferrates and Analogs. *Physchem* **2024**, *4*, 25–42. <https://doi.org/10.3390/physchem4010003>

Academic Editor: Anatoly L. Buchachenko

Received: 2 November 2023

Revised: 12 December 2023

Accepted: 13 December 2023

Published: 25 December 2023



Copyright: © 2023 by the authors. Licensee MDPI, Basel, Switzerland. This article is an open access article distributed under the terms and conditions of the Creative Commons Attribution (CC BY) license (<https://creativecommons.org/licenses/by/4.0/>).

1. Introduction

Magnetic resonance imaging (MRI) has emerged as a prominent, non-invasive and nonradioactive tool for diagnosing various diseases and/or testing human organ functions [1,2]. To aid diagnoses, it is often necessary to administer an imaging agent to improve the contrast [1,3]. This is especially true for imaging the brain or spine where small details are often key [4]. For example, Figure 1a illustrates the use of a contrast agent for the MRI of the brain. Specifically, the right side of Figure 1a shows a much clearer and more detailed picture with the use of a contrast agent in comparison with the one on the left, where no contrast agent is used. The current clinical MRI agents all contain a single paramagnetic metal ion in their center, with gadolinium (Gd) as the most frequently used metal so far in commercial contrast agents, e.g., Gd-DTPA (Magnevist[®], Schering AG, Berlin, Germany). These Gd-based agents are used in about one in three of MRI scans to improve the clarity of the images for the internal structures of the human body [4–6]. Often, the use of an MRI

contrast agent improves the visibility of inflammation, tumors, and blood vessels, or, in some cases, even blood flow or the real-time function of blood vessels. In turn, a better MRI image provides better medical diagnostic accuracy. For example, many detailed heart or brain abnormalities can be better assessed [4,6].

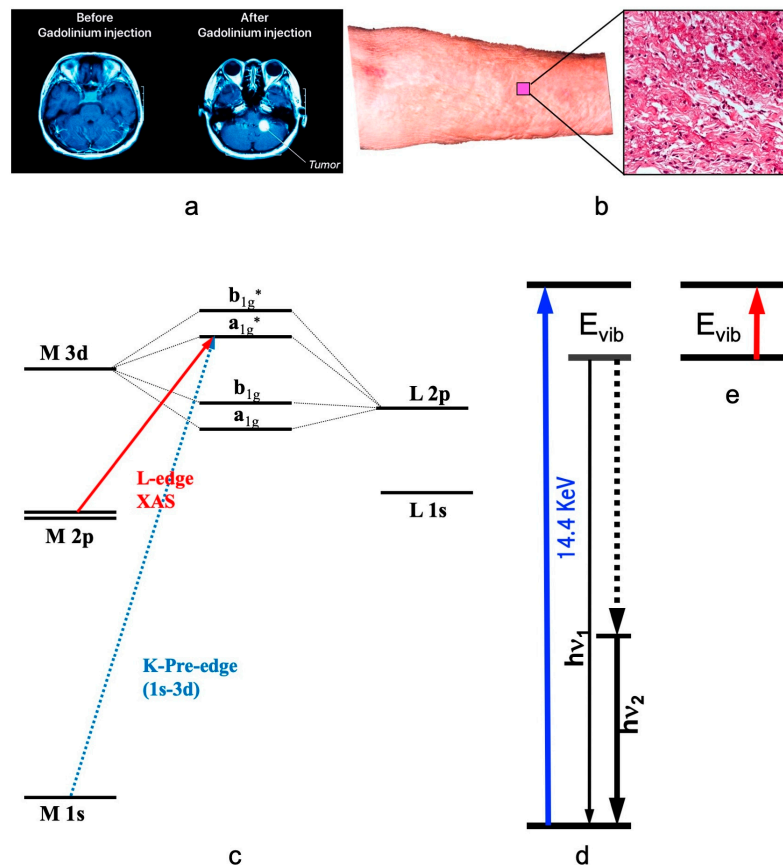


Figure 1. (a) The illustrative MRI images without (left) vs. with a contrast agent (right); (b) the skin surface and its microscopic profile of NFS; (c) illustrative K- and L-edge X-ray absorption spectroscopy (XAS) transitions and the associated energy levels; (d) nuclear resonant vibrational spectroscopy (NRVS) transitions which measure the vibrations indirectly but with many advantages; (e) infrared absorption spectroscopy (IR), which measures vibrations directly.

Although Gd contrast agents have proven to be invaluable, they are not without drawbacks. In extreme cases, these agents can lead to a serious disease called nephrogenic systemic fibrosis (NSF) [6–11]. An example of an NSF patients' skin appearance as well as the detailed view are shown in Figure 1b and its right insert. These are the Gd-related deposits. In 2010, synchrotron radiation (SR)-based X-ray fluorescence microscopy (SXRF) and extended X-ray absorption fine-structure spectroscopy (EXAFS) were used to chemically and spectroscopically characterize the Gd deposits in the skin from an NSF patient [8]. It was concluded that the Gd deposits in that NSF case consisted of a Gd-phosphate material with almost no Gd remaining coordinated to the original organic chelator [8]. One reason is that the Gd^{3+} ion has a very similar radius to that of Ca^{2+} (i.e., 1.07 Å for Gd^{3+} and 1.02 Å for Ca^{2+}) and can replace the Ca^{2+} in the human body and skin [8]. Therefore, Gd-DTPA or other Gd-based agents are still considered harmful in general [6–9,11–14], and hence safer alternative imaging contrast agents need to be explored.

From the entire periodic table, there are only a few elements that are considered suitable as MRI enhancement candidates. Specifically, they simultaneously need to have a high number of unpaired electrons, a long electronic relaxation time, and a stable oxidation state under the physiological conditions inside the human body. Hence, the suitable candidates include, for example, Gd(III) ($S = 7/2$), Eu(II) ($S = 7/2$), Fe(III) ($S = 5/2$),

and Mn(II) ($S = 5/2$). Among these, the Mn(II) ion is a bio-essential element and thus more compatible with biological cells than Gd(III). It also has a high electronic spin ($S = 5/2$) and a fast rate in water exchange, possessing almost ideal physical, chemical, and biological properties for MRI applications [15,16]. These properties led to two U.S. Food and Drug Administration (FDA)-approved contrast agents for clinical use, i.e., MnDPDP (DPDP = dipyridoxyl diphosphate; Teslascan[®]) and MnCl₂ (LumenHance[®]). However, all Mn complexes including MnDPDP are kinetically labile and susceptible to interaction with other metals such as Zn, Cu and Fe, etc. In particular, Mn(II) from these agents may be released from the contrast agents to the human body and cause problems, e.g., by replacing Zn(II) [17,18]. MnCl₂ in aqueous solution can exist as $[\text{Mn}(\text{H}_2\text{O})_6]^{2+}$ and Cl^- ions in the stomach. Even in a strong HCl environment, it does not tend to form the suspected $[\text{MnCl}_n]^{(n-2)-}$ complexes, which is very different from CuCl or AgCl. Although Mn(II) has much lower toxicity than Gd(III), the absorption of an excessive amount of Mn can still cause neurotoxicity. Other single-metal-centered coordination complexes also show various disadvantages and various potential toxic concerns.

These concerns may be addressed by incorporating Mn (or other proper metal ions including Gd) into the Prussian blue (PB) structure in the form of nanomaterials [19,20]. PB has extremely high formation constants (e.g., $K_f = 1.6 \times 10^{31}$ for PB vs. 10^{23} for Gd-DTPA) and, therefore, is much safer for medical use. For example, it is one of the most important medications on the World Health Organization's List of Essential Medicines [21]. In general, it has a chemical formula of $\text{Fe}^{\text{III}}_4[\text{Fe}^{\text{II}}(\text{CN})_6]_3 \cdot x\text{H}_2\text{O}$, with a cubic crystal lattice which has an atomic arrangement of $-\text{Fe}^{\text{II}}-\text{C}-\text{N}-\text{Fe}^{\text{III}}-\text{N}-\text{C}-\text{Fe}^{\text{II}}-$ in each dimension (similar to those shown in the references [19,20,22]). A quarter of Fe(II) centers along with CN^- ions have to be absent from the crystal lattice in order to maintain a ratio of $\text{Fe(III)}:[\text{Fe}^{\text{II}}(\text{CN})_6]^{4-} = 4:3$ to realize the electrical neutrality of PB [23]. This arrangement creates a void inside the structure that is filled by a varying number of H₂O molecules (i.e., $x = 1$ to 12). For PB-like analogs, such as the manganese cyanidoferrates $\text{K}_2\text{Mn}[\text{Fe}(\text{CN})_6]$ to be explored in this study, Mn:Fe = 1 is maintained instead, while a counterion of K^+ , or sometimes other monovalent ions, such as Li^+ , Na^+ , K^+ , Rb^+ , Cs^+ , Tl^+ , or $(\text{NH}_4)^+$, can be used to maintain the electrical neutrality for the whole compound.

These PB-like compounds, e.g., $\text{K}_2\text{Mn}[\text{Fe}(\text{CN})_6]$, have attracted a great deal of attention as potential MRI contrast agents in the past ten years [19,20,24] because: (1) the extremely high formation constant leads to an extremely stable complex [19,20], which in turn contributes to a much reduced risk of exposing the patients to the metal ions; (2) these complexes have a long blood circulation time, which is desirable for detailed imaging studies [25]; and (3) a given nanoparticle can form a superparamagnetic domain. Such a material can thus possess a much higher magnetic susceptibility as compared with the paramagnetic materials composed of single molecules. This property can produce a much higher MRI sensitivity. On the other hand, nanoparticles are still small enough to be freely transported inside the human bloodstream.

There are a few major scientific issues concerning $\text{K}_2\text{Mn}[\text{Fe}(\text{CN})_6]$ in general: (1) what are the oxidation states of the two metals inside the complex? That is, whether this complex has a Mn(II)/Fe(II), a Mn(II)/Fe(III), a Mn(III)/Fe(II) or a Mn(III)/Fe(III); (2) what are the electronic spin states (i.e., ls vs. hs, where ls = low spin and hs = high spin) of the two metal sites? (3) In PB, the ls-Fe(II) takes the C-bound position in the $[\text{Fe}(\text{CN})_6]^{4-}$ ion and the hs-Fe(III) takes the N-bound position in the $[\text{Fe}(\text{CN})_6]^{4-}$ ion. In $\text{K}_2\text{Mn}[\text{Fe}(\text{CN})_6]$, does the Mn take the positions for the original N-bound hs-Fe(III) sites or those for the C-bound ls-Fe(II) sites in comparison with PB? For such a simple complex, the chemical intuition seems to suggest that the tightly bound $[\text{Fe}(\text{CN})_6]^{4-}$ ions from the starting material of $\text{K}_4[\text{Fe}(\text{CN})_6]$ will remain the original Fe(II) ($S = 0$), while the complexed Mn can take the PB's hs-Fe(III) position and, in principle, be in different oxidation states (e.g., Mn(III) vs. Mn(II)) and/or different spin states (hs vs. ls) according to the Mn source. As the C-bound ls-Fe(II) in $[\text{Fe}(\text{CN})_6]^{4-}$ ion has an $S = 0$, the total spin in such PB-like complexes has the electronic spin of the N-bound metal alone—for instance, from the hs-Mn(II), $S = 5/2$.

Nevertheless, it appears to be very meaningful to use modern spectroscopies [26–35] to shed some light directly on these issues which are also critical for evaluating its suitability as an MRI agent [19,20].

SR-based X-ray absorption spectroscopy (abbreviated as XAS hereafter, Figure 1c) measures the electronic transition from a core shell to a valence shell. As XAS is sensitive to valence electrons and is element specific (related to core shell) at the same time, it is one of the best methods for investigating the oxidation state of a specific element in different chemical compounds or enzymes [27,29–32,36,37]. For the 3d transition-metal ions (e.g., Mn, Co or Fe ion), K-edge XAS uses a hard X-ray beam of >4000 eV to study the transitions of $1s \rightarrow 3d$, $\rightarrow 4p$ and \rightarrow continuum (Figure 1c, the transition designated by the dashed blue line). Although the information obtained from the K-edge XAS seems comprehensive [27,32–34,37], L-edge XAS [29–31,36,38,39] (Figure 1c, the transition designated by the solid red line) as well as L-edge RIXS or L-edge X-ray emission spectroscopy [40–43] have several advantages over the K-edge XAS for studying electronic structures such as oxidation states and spin states. These advantages include a direct probe of the ligand-metal bonding orbital (3d); a dipole-allowed $2p \rightarrow 3d$ transition (vs. $1s \rightarrow 3d$ in K-edge XAS); a better energy resolution (e.g., 0.1 eV vs. 1 eV); and a rich spectral multiplet which is specific to particular electronic structures and coordination environments [29–31,36,38,39].

Nuclear resonant vibrational spectroscopy (or NRVS for short) is another SR-based modern spectroscopic technique that was widely used by physicists, chemists, biochemists, and materials scientists. It measures the phonons, or, in other words, vibrational modes associated with the nuclear transition for a specific isotope, as illustrated in Figure 1d. The most frequently used NRVS to date is the ^{57}Fe NRVS which has a nuclear resonant transition at 14.4 keV [28,44–49]. In short, it is a scattering spectroscopy in general and a nuclear resonant scattering spectroscopy in particular. In comparison with the conventional infrared absorption spectroscopy (IR) [50] (Figure 1e), it measures vibrations indirectly but has several distinct advantages. The most prominent advantages include but are not limited to being isotope (e.g., ^{57}Fe) specific for studying complicated systems [28,48,49,51,52], having an almost zero background [28,48], and being able to obtain a theoretically calculable partial vibrational density of state (PVDOS) [28,45–47,53]. These advantages make it a better method in comparison with the laboratory-based IR [28,50], Raman [28] and laser-induced fluorescence (LIF) spectroscopies [54–56] as well as SR-based inelastic X-ray scattering (IXS) [28,57]. This modern spectroscopy became available in the mid 1990s, due to the development of the third-generation SR sources which provide the strong X-ray pulses with specific timing structure, advanced X-ray optics which lead to a monochromator with an 1 meV energy resolution to measure vibrations, and modern detectors which extract a weak nuclear scattering signal from the huge electronic scattering counts in the time domain, and in turn, it has pushed a great advancement in physics, chemistry, biochemistry and materials science, etc., for the past 28 years [45–49,52]. In chemistry and bioinorganic chemistry, for example, this technique has uncovered Fe-S/P/Cl, Fe-CO/CN/NO and Fe-H/D vibrational modes inside various inorganic complexes as well as dilute iron enzymes [28], and has thus become an excellent pinpointing tool to study iron-specific electronic and structural properties, including iron oxidation state(s) and coordination environments. For PB-like compounds, it can pinpoint the features attributable to the N-bound hs-Fe(III) or those to the C-bound ls-Fe(II) [22,28].

In this publication, the $\text{K}_2\text{Mn}[\text{Fe}(\text{CN})_6]$ complex was first measured and analyzed with the Mn and Fe L-edge XAS. For comparison, $\text{KFe}[\text{Co}(\text{CN})_6]$ as well as the reference samples ($\text{K}_4[\text{Fe}(\text{CN})_6]$ and $\text{K}_3[\text{Co}(\text{CN})_6]$) were also measured and analyzed with Fe and Co L-edge XAS. From the information obtained from these L-edge XAS measurements, $\text{K}_2\text{Mn}[\text{Fe}(\text{CN})_6]$ was confirmed to have an hs-Mn(II) bound to the $[\text{Fe}(\text{CN})_6]^{4-}$ ion in the N position in 6CN^- and an ls-Fe(II) bound to the 6CN^- in the C position. In comparison, $\text{KFe}[\text{Co}(\text{CN})_6]$ had an hs-Fe(II) bound to the in the N position and an ls-Co(III) bound to the C position. For NRVS, ^{57}Fe labelled $(\text{NH}_4)_2\text{Mg} [^{57}\text{Fe}(\text{CN})_6]$ and $\text{K}^{57}\text{Fe}[\text{Co}(\text{CN})_6]$ were first presented as the two standards to illustrate the nature of the two “peaks” in the

natural PB NRVS [22,28]. Then, non-labelled $\text{K}_2\text{Mn}[\text{Fe}(\text{CN})_6]$ was measured with regional NRVS where only the energy regions around the resonant peak and the Fe-CN vibrational peak were measured [22,28]. For discussion, the previously measured regional spectra for $\text{KGd}[\text{Fe}(\text{CN})_6]$ and $\text{KEu}[\text{Fe}(\text{CN})_6]$ [22] are also cited and compared with $\text{K}_2\text{Mn}[\text{Fe}(\text{CN})_6]$. From the NRVS results, we concluded that the nanoparticulated manganese cyanidoferrates $\text{K}_2\text{Mn}[\text{Fe}(\text{CN})_6]$ as well as $\text{KGd}[\text{Fe}(\text{CN})_6]$ and $\text{KEu}[\text{Fe}(\text{CN})_6]$ [22] have an ls-Fe(II) which occupies the C-bound position in the $[\text{Fe}(\text{CN})_6]^{4-}$ ion while the complexed Fe in $\text{K}^{57}\text{Fe}[\text{Co}(\text{CN})_6]$ has an hs-Fe(II) which takes the N-bound position to the $[\text{Co}(\text{CN})_6]^{3-}$ ion.

2. Experiments and Materials

2.1. L-Edge XAS Measurements

Iron (Fe), manganese (Mn) and cobalt (Co) L-edge XAS spectra (or L XAS) for $\text{K}_2\text{Mn}[\text{Fe}(\text{CN})_6]$ as well as for its comparison samples, reference samples or energy calibration samples were measured at the undulator beamline 4.0.2 at the Advanced Light Source (ALS) in Berkeley, California. As previously reported [29–31,36,38], powdered solid state samples were ground and pressed onto an ultrahigh vacuum (UHV)-compatible double stick carbon tape on the sample holder at room temperature, and loaded into a UHV-compatible measurement chamber, as illustrated in Figure 2a.

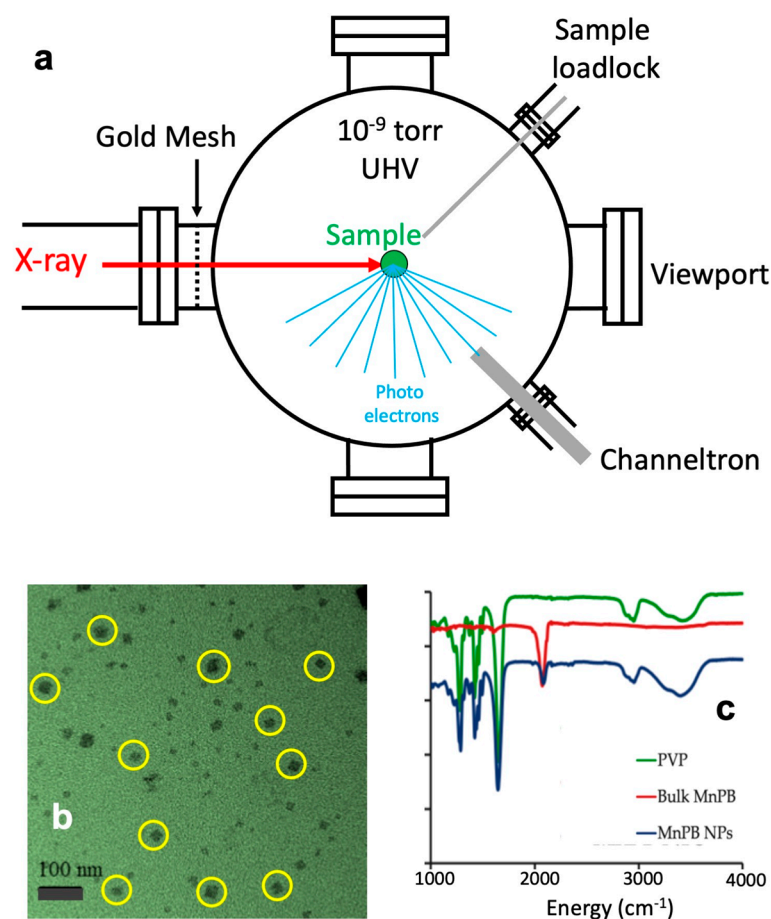


Figure 2. (a) A schematic drawing for 3d metal L-edge X-ray absorption spectroscopy (L XAS) measurement apparatus under ultrahigh vacuum (UHV); (b) a TEM image of the main sample—polyvinylpyrrolidone (PVP)-coated $\text{K}_2\text{Mn}[\text{Fe}(\text{CN})_6]$ nanoparticles (PVP-coated Mn-PB NPs for short). The yellow circles are used as an eye-guide; (c) IR spectra for PVP (green), bulk Mn-PB (red) and PVP-coated Mn-PB NPs (blue).

Although all the samples in this publication are not air sensitive, to better control the surface condition due to the fact that L-edge XAS is extremely surface sensitive [36,38],

the samples were ground, spread and mounted inside a nitrogen atmosphere glovebox maintained at an oxygen level of 1 ppm or less and then loaded into the UHV chamber via a vacuum-compatible loadlock (Figure 2a, upper right corner). While the X-ray beam scanned through the intended energy region(s), Fe or Mn or Co L-edge XAS spectra were recorded using a channeltron electron multiplier [29–31,36,38] (Figure 2a, lower right corner) to detect the emitted total photoelectrons whose intensity is proportional to the amount of X-ray absorption in the corresponding samples. Such spectra were further normalized to the incident radiation intensity monitored by using the photocurrent from a gold mesh (Figure 2a, left side). Energy calibration was performed with appropriate standards before and after each set of the measurements. We noticed that there was no absolute energy calibration standard in the previous reports; the following standards and energy positions were chosen for this publication: Fe L-edge calibrations used the lowest energy L_3 peak of Fe_2O_3 at 707.8 eV, Mn L-edge calibrations used the peak with the highest intensity of MnF_2 at 640.0 eV, while Co L-edge was calibrated to the first sharp peak of $Co(II)O$ at 778.8 eV. To reduce possible radiation damage, the monochromator's slits were set to 5 μm to decrease the beam flux to the order of 10^{11} photons/s and the X-ray beam obtained was further de-focused to $1 \times 1 \text{ mm}^2$ in its cross-section size on the sample. The energy resolution was at 0.1–0.2 eV.

2.2. NRVS Measurements

NRVS spectra were recorded using a published procedure [28,48,49,52] at SPring-8 beamlines BL09XU in Japan. A high-heat load monochromator (HMLM) produced 14.4 keV radiation with ~ 1.0 eV energy resolution, and a high energy resolution monochromator (HRM) (with crystals of Ge(422) and Si(975) $\times 2$) [58,59] subsequently produced 14.4 keV radiation with 0.8 meV energy resolution, suitable for measuring vibrations. The beam flux was $\sim 1.8 \times 10^9$ photons/s at the time of the measurements. During NRVS measurements, the samples were maintained at a cryogenic temperature (e.g., 10K at the temperature sensor) using a liquid helium cryostat. However, the real sample temperatures [28] derived from anti-Stoke/Stoke intensity ratios from the NRVS spectra were found to be 40–60 K instead. As illustrated in Figure 1d, while an incident X-ray beam (thick blue line) scans through the energy region of interest to cover the nuclear transition (e.g., 14.4 keV for ^{57}Fe) and the associated vibrations (e.g., Fe-CN), the extremely narrow bandwidth for the nuclear back radiation $h\nu_1$ (thin black line) can be used as an excellent intrinsic "spectrometer" to "measure" the scattered energy in precision while the signal vs. background can be distinguished in the time domain, just like LIF does [54–56]. NRVS thus does not need a low-throughput (diffraction-based) spectrometer for filtering the scattered beam and thus has a much higher photon in and photon out efficiency in comparison with IXS which also measures vibrations [28]. The total intensities collected from both the direct nuclear fluorescence at $h\nu_1$ (thin black line) and the internally converted electron K shell fluorescence at $h\nu_2$ (short, thick black line) were recorded with a 2×2 avalanche photodiode (APD) array [28,52]. This signal vs. the vibrational energy (E_{vib}) forms a raw NRVS spectrum. NRVS has many prominent advantages, including being able to be converted to a partial vibrational density of state (PVDOS). The raw NRVS \rightarrow PVDOS conversion may be obtained with the PHOENIX software package or a web-based version of PHOENIX [28,53]. The detailed information about the NRVS instruments, measurement and analysis is the same as that published widely [28,45–49,52,53] and will not be repeated here.

2.3. Sample Preparation and Basic Characterization

The main sample, polyvinylpyrrolidone (in brief, PVP, chemical formula = $C_{10}H_{15}NO_3$)-coated $K_2Mn[Fe(CN)_6]$ nanoparticles (Mn-PB NPs for short), was prepared with a procedure as published earlier [19,20] and described in brief in the supporting information (SI). The proposed structure for Mn-PB is similar to the PB except the original hs-Fe(III) sites were substituted with Mn and an Mn:Fe = 1:1 ratio was maintained while K^+ was used to balance the extra negative charge. PB was used as a platform and PVP was used as a coating

agent to prevent the Mn-PB nanoparticles from agglomerating and to improve its chemical stability and biological compatibility. The as-synthesized nanoparticles were dialyzed in a semi-permeable membrane in distilled water. Any unbound PVP should effectively be removed during this process. From a transmission electron microscopy (TEM) image, as shown in Figure 2b, the PVP-coated Mn-PB NPs were 5–20 nm in size and were well separated from one another. No chunks of PVP or mixture of PVP and PB were observed. Characterization and in vitro as well as in vivo MRI studies of the Mn-PB NPs were similar to the one reported previously [60].

The IR spectra of PVP-coated Mn-PB NPs (blue), bulk Mn-PB (red) and PVP (green) were measured and are shown in Figure 2c. The IR spectra of the PVP-coated Mn-PB NPs and the uncoated Mn-PB both showed characteristic C≡N stretching vibrations at $\sim 2073\text{ cm}^{-1}$ and 2082 cm^{-1} (not appearing as separate peaks in Figure 2c due to the wide plotting range to show all the features). The IR spectrum for Mn-PB NPs showed additional bands at 1650 cm^{-1} , 1421 cm^{-1} and 1280 cm^{-1} , which overlap with the bands for PVP. This and the TEM photo in Figure 2b showed that PVP was covering the Mn-PB NPs' surface. The presence of water was also confirmed by the peak at 3465 cm^{-1} (O-H stretching) and is consistent with the fact that PVP is hydrophilic. The thickness for the PVP coating is estimated to be less than 10 nm, which can let at least 98% of the soft X-ray ($>630\text{ eV}$) pass through its layer and reach the Mn-PB NPs samples. For NRVS, the transmission of X-ray at 14.4 keV of the 10 nm PVP is close to 100%.

The structural analogs, $\text{KGd}[\text{Fe}(\text{CN})_6]$ and $\text{KEu}[\text{Fe}(\text{CN})_6]$, were synthesized with the same procedure described in supporting information (SI) [19,20] but with Eu, Gd sources (instead of a Mn source) introduced to the $\text{K}_4[\text{Fe}(\text{CN})_6]$ complex. The ^{57}Fe -enriched $\text{K}^{57}\text{Fe}[\text{Co}(\text{CN})_6]$ was produced with a similar procedure by introducing a ^{57}Fe source (e.g., $^{57}\text{FeCl}_2$) to the $\text{K}_3[\text{Co}(\text{CN})_6]$ complex alternatively. The NRVS spectrum for $(\text{NH}_4)_2\text{Mg}[\text{Fe}(\text{CN})_6]$ was directly cited from the previous publications [22,28]. The comparison samples in this study, MnF_2 , $\text{K}_3[\text{Co}(\text{CN})_6]$, FeO , $\text{K}_4[\text{Fe}(\text{CN})_6]$, and $\text{K}_3[\text{Fe}(\text{CN})_6]$, were purchased from commercial sources and used without further processing. Additional energy calibration samples, Fe_2O_3 , and CoO , were also purchased from commercial sources and used without further processing.

For better control of their surface conditions, all the samples, include the main sample and all the comparison, reference and energy calibration samples were stored inside an N_2 based glovebox for over 7 days before loading into the measurement chamber for L XAS measurement. For NRVS measurement, this step becomes unnecessary.

3. Results and Discussion

In general, the oxidation state is one of the most-pursued chemical properties. Resolved oxidation states or electron/charge densities have helped the understanding of many chemical processes [36,38], while an unresolved oxidation state has contributed to many longstanding controversies in history [61–65]. This is especially true for transitional metal complexes [36,38]. L-edge XAS for 3d metals which measures the $2p \rightarrow 3d$ transition is one of the best methods for investigating the oxidation states and electronic spin state via the L_3 absorption edge positions or their centroid energies. For example, L XAS exhibits an approximate 2 eV change in the L_3 centroids per oxidation state change (eV/oxi) for the Mn complexes and 0.9 eV/oxi for Ni complexes [29,36,66]. The ls-Ni(II) also has a higher L_3 centroid than the hs-Ni(II). For Mn complexes, the branching ratio of $\text{L}_3/(\text{L}_3 + \text{L}_2)$ has also sometimes been used to determine the Mn oxidation states, where the L_3 and L_2 mean the integrated intensities at the L_3 and L_2 edges, respectively [36,66]. These L-edge centroids are often sufficient to assign the oxidation states.

The spectral multiplets are more essential to identify a metal's oxidation states, electronic spin states and its coordination symmetries [36,38,66–69]. The match of their spectral multiplets in two spectra indicates that two samples have the same metal sites (or at least extremely similar metal sites). Due to its fingerprint-like multiplets, L-edge XAS is sensitive and has been widely used to identify the oxidation states, spin states and other information

mentioned above for metal centers in various 3d transition-metal complexes and metalloenzymes [36,38]. For example, it has been used to identify Ni(I, II, III) and even Ni(II) with different electronic spin states (hs vs. ls) successfully [37–39].

3.1. Manganese L-Edge XAS

The Mn L-edge XAS for our nanoparticulated $\text{K}_2\text{Mn}[\text{Fe}(\text{CN})_6]$ is shown in Figure 3a. It shows an almost identical multiplet feature in both the L_3 and L_2 regions as the one for MnF_2 (Figure 3b). The latter is well known to have an hs-Mn(II) center [70,71], making our assignment of the Mn center in $\text{K}_2\text{Mn}[\text{Fe}(\text{CN})_6]$ as an hs-Mn(II) rather reliable. In comparison with the Mn L-edge XAS for various other complexes with various Mn oxidation states and spin states in previous publications [67,70,71], our Mn L-edge XAS for $\text{K}_2\text{Mn}[\text{Fe}(\text{CN})_6]$ (Figure 3a) is similar to that of MnO (such as the one in Figure 1 of the reference [67]) and MnF_2 (such as the one in Figure 2 of the reference [70]) which have an hs-Mn(II). On the other hand, it is very different from those of the other Mn complexes with oxidation states ranging from +3 to +7 (the ones in [67]) or from more covalent Mn(II) complexes (the ones in [70]). In comparison with Figure 3(a) and (b) (oxidation state = +2), most of the L-edge XAS for the compounds with oxidation state = +3 to +7 [67] have higher L_3 peak centroids, reflecting the correlation between the oxidation state and the L_3 centroid. These observations are consistent with the discussions in the associated references [36,67,68,70].

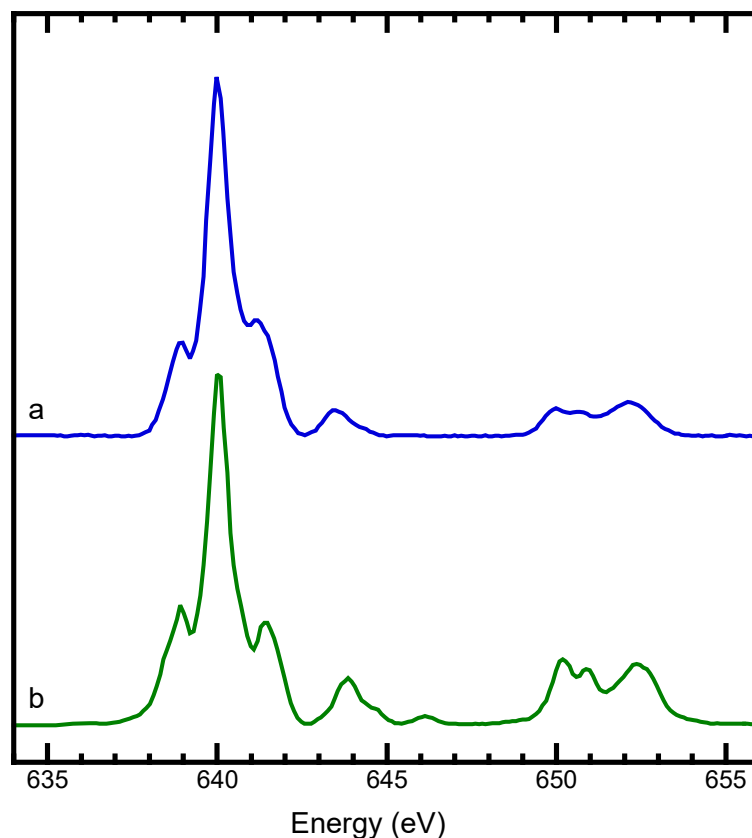


Figure 3. Mn L-edge XAS for $\text{K}_2\text{Mn}[\text{Fe}(\text{CN})_6]$ (a) and MnF_2 (b).

According to a previous publication (Figure 3 in [70]), the ls-Mn(II) in $[\text{Mn}(\text{CN})_6]^{4-}$ ion [70] shows a sharp peak at 638.6 eV which is well separated from the rest of the L_3 multiplets. This is a quite unique feature for a $[\text{Mn}(\text{CN})_6]^{4-}$ [70]. The fact that $\text{K}_2\text{Mn}[\text{Fe}(\text{CN})_6]$ does not have this feature (especially the lack of a “pre- L_3 ” peak at 638.6 eV) indicates the Mn(II) in $\text{K}_2\text{Mn}[\text{Fe}(\text{CN})_6]$ is not in the C-bound position as that in the $[\text{Mn}(\text{CN})_6]^{4-}$ ion. Although there is no particular L XAS report found for $[\text{Mn}(\text{CN})_6]^{3-}$, previous reports revealed that there was about a 2 eV L_3 centroid shift between Mn(II) and Mn(III) [36,72], excluding the possibility of a $[\text{Mn}(\text{CN})_6]^{3-}$ site as well. Taken as a whole, our L XAS data

show that the complexed Mn is not in the C-bound position in 6CN^- , or in other words, it could occupy the position of the N-bound hs-Fe(III) site in PB. This in turn implies that Fe in $\text{K}_2\text{Mn}[\text{Fe}(\text{CN})_6]$ should remain in the C-bound position in the $[\text{Fe}(\text{CN})_6]^{4-}$ ion.

3.2. Cobalt L-Edge XAS

$\text{K}_2\text{Mn}[\text{Fe}(\text{CN})_6]$ was prepared by introducing a Mn(II) source (i.e., MnCl_2) into $\text{K}_4\text{Fe}(\text{CN})_6$ to form a PB analog compound (SI) [19,20]. According to L XAS (Figure 3a vs. Figure 3b, Figures S2 and S3), Mn is found to be in the N-bound position in PB. In an “opposite” approach, a $^{57}\text{Fe}(\text{II})$ source (i.e., $^{57}\text{FeCl}_2$) was complexed into the $[\text{Co}(\text{CN})_6]^{3-}$ ion to form an alternative PB analog compound of $\text{K}^{57}\text{Fe}[\text{Co}(\text{CN})_6]$ where Co should remain in the C-bound position in the $[\text{Co}(\text{CN})_6]^{3-}$ ion. Therefore, Co vs. Mn L XAS can provide a meaningful comparison insight into the two different cases. For this purpose, Figure 4 shows the Co L XAS for the comparison samples $\text{K}^{57}\text{Fe}[\text{Co}(\text{CN})_6]$ (Figure 4a) and the reference sample $\text{K}_3[\text{Co}(\text{CN})_6]$ (Figure 4b).

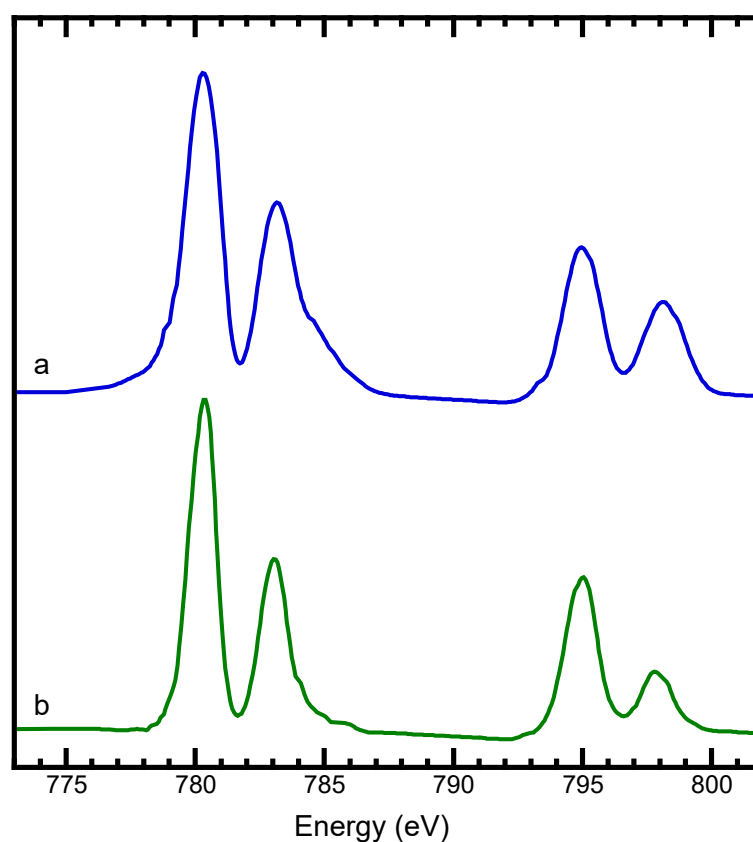


Figure 4. Co L-edge XAS for $\text{K}^{57}\text{Fe}(\text{II})\text{Co}(\text{III})(\text{CN})_6$ (a) and $\text{K}_3\text{Co}(\text{III})(\text{CN})_6$ (b).

First, the previously reported L XAS result on $\text{K}_3[\text{Co}(\text{CN})_6]$ (such as the one in Figure of the reference) [73] is satisfactorily reproduced in Figure 4b, establishing a good reference spectrum for the ls-Co(III) in $[\text{Co}(\text{CN})_6]^{3-}$. The fact that the Co L XAS spectrum for $\text{KFe}[\text{Co}(\text{CN})_6]$ (Figure 4a) has an overall resemblance as well as the same characteristic feature for ls-Co(III) in $\text{K}_3[\text{Co}(\text{CN})_6]$ (Figure 4b) shows that the Co in $\text{KFe}[\text{Co}(\text{CN})_6]$ is in the C-bound position in $[\text{Co}(\text{CN})_6]^{3-}$ [73]. There are some minor differences in the intensity ratio and peak width, but the overall features resemble each other pretty well. We noticed that our spectrum for $\text{K}_3[\text{Co}(\text{CN})_6]$ (Figure 4b) also has a slight difference in peak positions in comparison with the previous reports (such as the one in Figure 2 of the reference [73]), probably due to the minor difference in energy calibrations.

On the other hand, when comparing with L XAS reports for other Co complexes in previous publications [73–77], our Co L XAS for $\text{KFe}[\text{Co}(\text{CN})_6]$ appears to be very

different from them. In particular, the Co L XAS for $\text{KFe}[\text{Co}(\text{CN})_6]$ has a very different multiplet from the L XAS for the Co in the N-bound position in other PB analogs, such as in $\text{ACo}[\text{Fe}(\text{CN})_6] \cdot x\text{H}_2\text{O}$ ($A = \text{Na}$ or K) (the spectra in Figure 2 of the reference [73]). This rules out the possibility that the Co in $\text{KFe}[\text{Co}(\text{CN})_6]$ is in the N-bound position to the $[\text{Fe}(\text{CN})_6]^{4-}$ ion. In addition, its spectroscopic feature is also very different from the Co L XAS features of various Co(II), ls-Co(III) and hs-Co(III) complexes in previous publications [73–77]. In short, the L XAS for $\text{KFe}[\text{Co}(\text{CN})_6]$ in Figure 4a only resembles the L-edge XAS of an ls-Co(III) in a $[\text{Co}(\text{CN})_6]^{3-}$ ion (e.g., Figure 4b or the reported spectrum in [73]). The Co(III) in a strong ligand field created from the 6CN^- ions has to be an ls-Co(III) instead of an hs-Co(III). This observation is not unexpected, just like the Fe is an ls-Fe(II) in $\text{K}_2\text{Mn}[\text{Fe}(\text{CN})_6]$.

3.3. Iron L-Edge XAS

Sections 3.1 and 3.2 present a comparison of L XAS features between Mn and Co—the former is in the N-bound position while the latter is in the C-bound position. This in turn puts their Fe in different positions in the PB structure and the two complexes should have different Fe L XAS spectra.

In this section, the Fe L XAS of $\text{K}_2\text{Mn}[\text{Fe}(\text{CN})_6]$ (Figure 5a, solid line) and its comparison complex $\text{KFe}[\text{Co}(\text{CN})_6]$ (Figure 5b, solid line) are evaluated. $\text{K}_2\text{Mn}[\text{Fe}(\text{CN})_6]$ shows a typical spectral feature of an ls-Fe(II) especially when it is compared with that of the ls-Fe(II) in $\text{K}_4\text{Fe}(\text{CN})_6$ (Figure 5a, dashed line, or as in Figure 2a of the reference [78]). This spectral feature is also similar to those of several other ls-Fe(II) complexes in reference [79]. This is no surprise because these cited complexes all have CO or CO/CN ligands, and both CO and CN are very similar, strong ligands [80–82]. On the other hand, the Fe L XAS of $\text{K}_2\text{Mn}[\text{Fe}(\text{CN})_6]$ (Figure 5a, solid line) does not have any similarity with the Fe(0) in $(\text{NEt}_4)_2\text{Fe}_0(\text{CO})_3(\text{CN})_2$ or Fe(I) in $\text{Fe}(\text{pdt})(\text{PMe}_3)(\text{CN})(\text{CO})_4$ in the same reference [79] or Fe(III) in other references, including $\text{FeO}(\text{OH})_2$ [83], Fe_2O_3 [84], FeF_3 [84], FeNO_3 [85]. In particular, the Fe L XAS for the ls-Fe(III) in $\text{K}_3[\text{Fe}(\text{CN})_6]$ (Figure 5c) has a prominent sharp peak at ~ 706 eV, while Fe(II) in $\text{K}_4[\text{Fe}(\text{CN})_6]$ or $\text{K}_2\text{Mn}[\text{Fe}(\text{CN})_6]$ (Figure 5a) does not have this feature. This stand-alone peak is the major characteristic feature of the d^5 ls-Fe(III) [78,86]—the only difference between different d^5 ls-Fe(III) complexes is how far this peak is from the highest L_3 peak. In addition to the re-measurement (Figure 5c), a published L XAS spectrum for $\text{K}_3[\text{Fe}(\text{CN})_6]$ can also be found from Figure 2b of the reference [78]. From the comprehensive comparison, $\text{K}_2\text{Mn}[\text{Fe}(\text{CN})_6]$ certainly has an ls-Fe(II) feature rather than an ls-Fe(III) feature [86]. We, therefore, assign the comparison complex $\text{KFe}[\text{Co}(\text{CN})_6]$ to have an hs-Fe(II) in the N-bound position.

The comparison between the Mn/Fe L-edge XAS for $\text{K}_2\text{Mn}[\text{Fe}(\text{CN})_6]$ vs. Fe/Co L-edge XAS for $\text{KFe}[\text{Co}(\text{CN})_6]$ provides the readers with a clear understanding and an overall picture about the electronic properties for Mn, Fe, and Co. Specifically, the ls-Fe(II) in the C-bound position (Figure 5a) is consistent with the hs-Mn(II) in the N-bound position (Figure 3a) for $\text{K}_2\text{Mn}(\text{II})[\text{Fe}(\text{II})(\text{CN})_6]$ and the hs-Fe(II) in the N-bound position (Figure 5b) is consistent with the ls-Co(III) in the C-bound position (Figure 4a) for $\text{KFe}(\text{II})[\text{Co}(\text{CN})_6]$.

Photoreduction in SR beam is often an issue for L-edge XAS measurements because the beam intensity is high, while the soft X-ray penetration depth is very small [87]. For example, Colison et al. [86] found that $\text{K}_3[\text{Fe}(\text{CN})_6]$ or $[\text{Co}(\text{acac})_3]$ can be photo reduced from Fe(III) to Fe(II) species in 26 min or from Co(III) to Co(II) species in 20 min. To ensure that the Mn(II), Co(III) and Fe(II) in our samples were not produced from photoreduction (or oxidation), we used a heavily defocused beam of $1 \times 1 \text{ mm}^2$ in the beam size to greatly reduce the beam brightness and thus the photoreduction rate (by 2–3 orders) in order to prevent or at least minimize such a problem. In addition, a reduced beam flux was also obtained by setting much narrower beam slits as described in detail in the experimental section. To further evaluate the issue, we also quickly scanned on fresh points and frequently changed the measurement spots using a beam size of $0.5 \times 0.5 \text{ mm}^2$ and a three times increased beam flux (and thus 12 times increased beam brightness). No

photoreduction has been found for the complexes subjected to this testing condition, let alone under the real measurement condition. For example, we did not see any Fe(III), Mn(III) or Co(II) even in the first 1 min of each rapid scan on fresh points under the increased beam brightness. We did perform a few series of repeated testing scans in several spots and did not find any change in the spectral features during the whole time periods of over 3–5 h each. Nevertheless, all the L-edge XAS spectra presented in this study are only from individual scans of fresh points.

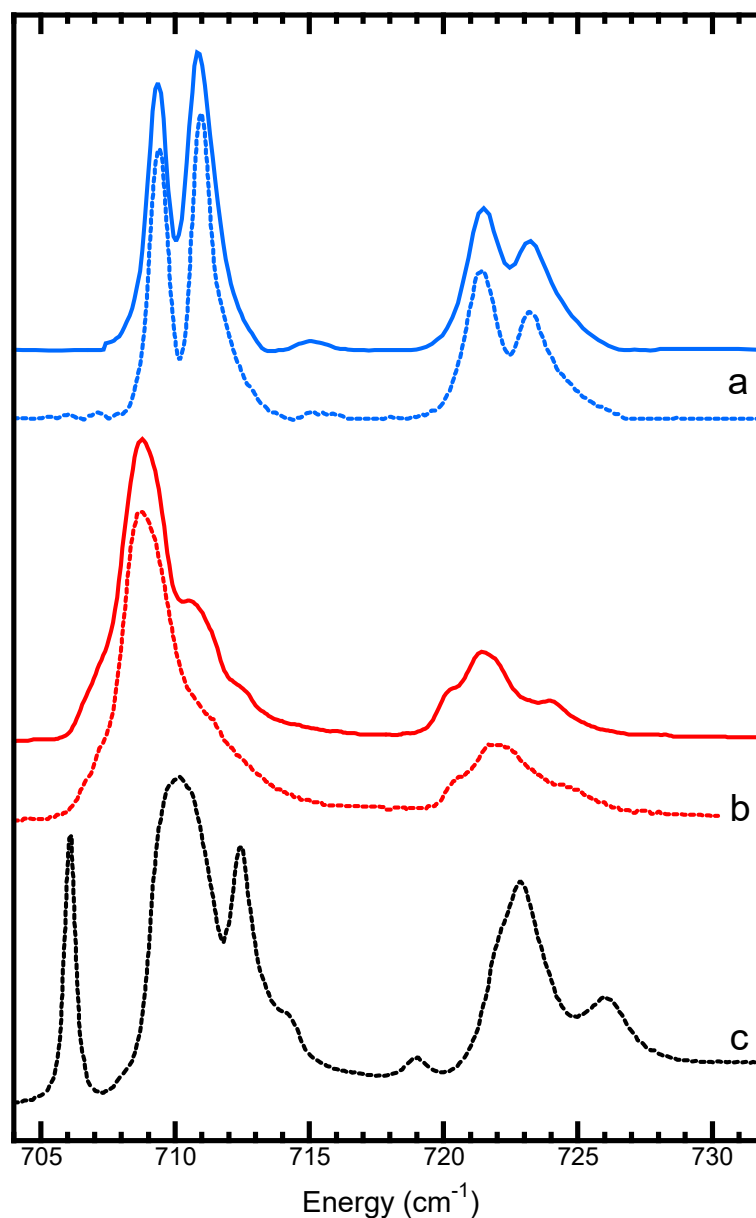


Figure 5. Fe L-edge XAS for $K_2Mn[Fe(CN)_6]$ (a) (solid line); $K_4[Fe(CN)_6]$ (a) (dashed line); $KFe[Co(CN)_6]$ (b) (solid line); FeO (b) (dashed line) and $K_3Fe(III)(CN)_6$ which has a sharp characteristic peak at 706 eV (c). The complexes in (a) have an *ls*-Fe(II), the ones in (b) have an *hs*-Fe(II), the one in (c) has an *ls*-Fe(III).

In short, the comprehensive L XAS analysis of Mn, Co, Fe inside $K_2Mn[Fe(CN)_6]$ as well as its comparison complex $KFe[Co(CN)_6]$ provides site-specific information on the oxidation states and spin states for these metals, which is critical when evaluating the new, non-gadolinium MRI contrast agents. In particular, our L XAS indicates that

$K_2Mn[Fe(CN)_6]$ contains an *hs*-Mn(II) and an *ls*-Fe(II), leading to a total spin per molecule of 5/2. This is suitable for an MRI agent.

3.4. ^{57}Fe NRVS

Since L-edge XAS and IR measurements are surface-sensitive methods, bulky sensitive ^{57}Fe -specific NRVS is an excellent addition to evaluate the Fe information in various PB-like complexes. Similar to other vibrational spectroscopies, NRVS is sensitive to oxidation states and has been widely used to assign the oxidation states for ^{57}Fe sites in different complexes and enzymes [28,48,49,51]. It also provides the ligand identity and symmetry around the ^{57}Fe site(s) [28]. For PB or PB-like compounds, NRVS can also indicate whether the spectral feature is from the Fe in the C-bound position in $[Fe(CN)_6]^{4-}$ or from the off-sphere N-bound position [22,28].

The PB NRVS has two major peaks (Figure 6a, green) [22,28]: (1) the strong interactions between the *ls*-Fe(II) and 6 CN^- ions, which leads to a sharp peak at 594 cm^{-1} ; and (2) the weaker interaction between the off-sphere *hs*-Fe(III) and the $[Fe(CN)_6]^{4-}$ ion (via Fe...N interactions), which produces an additional broad hump at $120\text{--}280\text{ cm}^{-1}$. Please note that the sharp peak position was mentioned in several previous publications [28,44] at 602 cm^{-1} , but it appears at 594 cm^{-1} [22] with the calibration method used by our research team (380 cm^{-1} for the Fe-Cl stretch peak in $(Et_4N)[FeCl_4]$ [28]). Although we realize that there are different energy calibration standards employed by different research teams with no effort made thus far to unify the calibration standards among different teams, using one standard in one research team is meaningful.

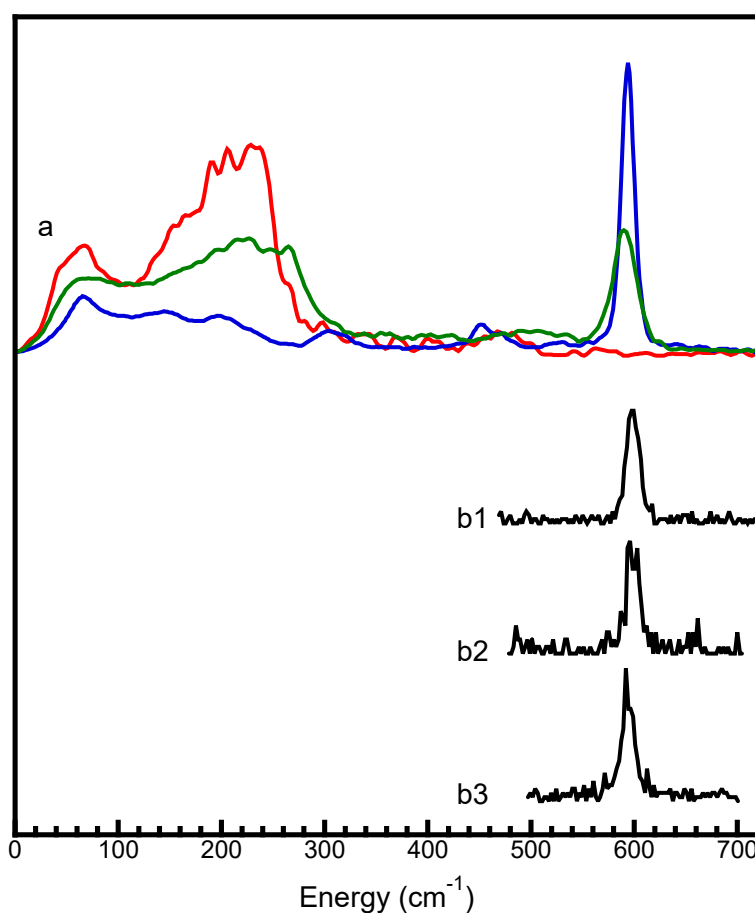


Figure 6. (a) NRVS spectra for ^{57}Fe -enriched PB (green), $(NH_4)_2Mg(II)-[^{57}Fe(II)(CN)_6]$ [44] (blue) and $K^{57}Fe(II)[Co(III)(CN)_6]$ (red); (b1–b3) NRVS peaks of $500\text{--}700\text{ cm}^{-1}$ for $K_2Mn(II)[Fe(II)(CN)_6]$ (b1), $KEu(III)[Fe(II)(CN)_6]$ (b2) and $KGd(III)[Fe(II)(CN)_6]$ (b3).

To further illustrate the origin of each peak (or hump), either the C-bound ls-Fe(II) or the N-bound hs-Fe(III) in PB can be “substituted” with another metal, leaving only one site labelled with ^{57}Fe . This approach creates two site-specific complexes: one is our comparison sample $\text{K}^{57}\text{Fe}[\text{Co}(\text{CN})_6]$. Its NRVS has no peak at or around 594 cm^{-1} at all but has a lower energy hump at $120\text{--}280\text{ cm}^{-1}$ (the red curve in Figure 6a). Another complex is $(\text{NH}_4)_2\text{Mg}(\text{II})[\text{Fe}(\text{II})(\text{CN})_6]$ [44] with a $[\text{Fe}(\text{CN})_6]^{4-}$ ion that is weakly bound to Mg. This complex has one strong NRVS peak at 594 cm^{-1} (the blue curve) but almost no hump at $120\text{--}280\text{ cm}^{-1}$. These NRVS spectra well illustrate how NRVS feature(s) can be used to confidently answer the question about the locations of their Fe sites in the corresponding PB analog compounds, i.e., in the C-bound position or the N-bound position.

Since $\text{K}_2\text{Mn}[\text{Fe}(\text{CN})_6]$ is not ^{57}Fe labelled, its NRVS thus has a very weak signal (2% ^{57}Fe in the natural abundance samples vs. 100% ^{57}Fe in the enriched samples). Therefore, measuring a full NRVS scan is out of the question. We instead only scanned a narrow region around the nuclear resonant peak at $E_{\text{vib}} = 0 (\pm 40\text{ cm}^{-1})$ and that around the sharp peak at $\sim 594\text{ cm}^{-1}$ (e.g., $380\text{--}700\text{ cm}^{-1}$ —the presentation range here is a bit less) [22,28]. Although the exact peak position for this sharp peak cannot be precisely located due to the skip-scan operation (jumping from the nuclear resonant peak region to the targeted sharp peak region) [22,28], the obtained peak feature is sharp and clear. The energy positions are less than $\pm 1\text{ meV}$ from the peak position at 594 cm^{-1} (Figure 6b1–b3 vs. Figure 6a), while the skip-scan uncertainty can be as large as 1.5 meV . This indicates the presence of a C-bound ls-Fe(II) in $[\text{Fe}(\text{CN})_6]^{4-}$, confirming the assignment based on the L-edge XAS measurements. This shows that a C-bound ls-Fe(II) is true for the bulk of the sample of $\text{K}_2\text{Mn}[\text{Fe}(\text{CN})_6]$, not just on its surface (L XAS).

Previously measured partial NRVS spectra for two unenriched samples $\text{KEu}[\text{Fe}(\text{CN})_6]$ and $\text{KGd}[\text{Fe}(\text{CN})_6]$ were also added to Figure 6b2,b3 for comparison—both of them also had a clear feature for a characteristic peak for the C-bound ls-Fe(II) in $[\text{Fe}(\text{CN})_6]^{4-}$ (around 594 cm^{-1}). On the other hand, the lack of a sharp NRVS peak at or around $\sim 594\text{ cm}^{-1}$ shows that the comparison complex $\text{K}^{57}\text{Fe}[\text{Co}(\text{CN})_6]$ does not have a C-bound ls-Fe(II). The NRVS comparison further indicates that the complexed element stayed in the N-bound position, which is consistent with the Mn, Co and Fe L XAS results. For reference, in a previous publication [22], ^{151}Eu and ^{57}Fe NRVS were used to measure $\text{KEu}[\text{Fe}(\text{CN})_6]$ vs. $\text{Eu}[\text{Fe}(\text{CN})_6]$ and to conclude the complexed metal (Eu) remains in the N-bound position in PB analogs.

In addition, NRVS can also identify whether the Fe is an Fe(II) or an Fe(III) [22]. In particular, as shown in, the Fe(III)–(CN) $_6$ interaction had a much lower energy position (at 516 cm^{-1}) and a much wider peak (32 cm^{-1} in FWHM) than the Fe(II)–(CN) $_6$ had (at 594 cm^{-1} with a 14 cm^{-1} FWHM). In general, this trend is not a surprise for complexes with CN or CO ligands [78,81,82,88,89]. In comparison, $\text{K}_2\text{Mn}[\text{Fe}(\text{CN})_6]$ indeed has an ls-Fe(II), not an ls-Fe(III) from NRVS.

4. Conclusions

In this publication, we have conducted detailed measurements of L-edge XAS on Mn and Fe, respectively, for the nanoparticulate PB analog $\text{K}_2\text{Mn}[\text{Fe}(\text{CN})_6]$ that has been synthesized and evaluated as a potential MRI agent [19,20]. The results obtained from such L XAS experiments allow us to unambiguously conclude that $\text{K}_2\text{Mn}[\text{Fe}(\text{CN})_6]$ has an hs-Mn(II) bound to N and an ls-Fe(II) bound to C in the PB structure. For comparison, Co and Fe L XAS on $\text{KFeCo}[(\text{CN})_6]$ showed that it had an hs-Fe(II) surrounded by N and an ls-Co(III) surrounded by C in the PB structure. Accordingly, K^+ ions have to be incorporated into the structure to maintain electroneutrality of the chemical formula and a ratio of Mn:Fe = 1:1 or Fe:Co = 1:1 for the corresponding complexes.

To rule out the possible issues of the surface effect, the bulk-sensitive ^{57}Fe NRVS study was also performed for $\text{K}_2\text{Mn}[\text{Fe}(\text{CN})_6]$ and its reference samples $\text{KEu}[\text{Fe}(\text{CN})_6]$ and $\text{KGd}[\text{Fe}(\text{CN})_6]$. The NRVS results were consistent with the above conclusions obtained from the surface-sensitive L XAS.

In addition to the evaluation of the relaxivity properties of $K_2Mn[Fe(CN)_6]$ to assess its suitability as a prime candidate for the next-generation non-gadolinium MRI agent, the current studies well illustrate the many significant advantages of using L XAS and NRVS in combination on the same sample to reveal site-specific information for nanoparticulate PB analog complexes or other complexes in general.

5. Future Work

In the future, it will be interesting to observe whether the so-called coordination isomers of this or similar complex(es) or certain types of solid-solutions where Mn(II) and Fe(II) ions (or other pairs of metals) are partitioned between the C-bound and the N-bound positions in PB analogs can be prepared if one uses a one-pot self-assembly synthesis involving stoichiometric amounts of Fe(II), Mn(II), and CN^- .

Supplementary Materials: The following supporting information can be downloaded at: <https://www.mdpi.com/article/10.3390/physchem4010003/s1>: Summary of Sample Preparation Procedures.

Author Contributions: H.W., A.T.Y. measured and analyzed L-edge XAS at ALS BL4.0.2; S.D.H. provided the samples; S.P.C. organized and academically advised the research; H.W., Y.Y., L.L. measured and analyzed ^{57}Fe NRVS; H.W. and S.D.H. wrote and revised the manuscript. All authors have read and agreed to the published version of the manuscript.

Funding: This work was supported by NIH grant R01-GM-65440 (to S.P.C., for NRVS and L XAS).

Data Availability Statement: Data are contained within the article and Supplementary Materials.

Acknowledgments: L-edge XAS measurements were carried out at ALS BL4.0.2. ALS was supported by the Director, Office of Science, Office of Basic Energy Sciences, U.S. Department of Energy under Contract No. DE-AC03-76SF00098. NRVS was measured at SPring-8 BL09XU (via JASRI proposal 2018A1409, 2018B1379, and 2019A1259). We also thank Murthi S. Kandanapitiye in Kent State U for his assistance in synthesizing the PB analog samples in this study.

Conflicts of Interest: The authors declare no conflicts of interest. The funders had no role in the design of the study; in the collection, analyses, or interpretation of data; in the writing of the manuscript; or in the decision to publish the results.

References

1. Geraldes, C.F.G.C.; Laurent, S. Classification and basic properties of contrast agents for magnetic resonance imaging. *Contrast Media Mol. Imaging* **2009**, *4*, 1–23. [CrossRef] [PubMed]
2. Tınaz, Ş.; Stern, C.E. Principles of Functional Magnetic Resonance Imaging and its Applications in Cognitive Neuroscience. *Turk. J. Neurol.* **2005**, *11*, 8–26.
3. Parizel, P.M.; van den Hauwe, L.; De Belder, F.; Van Goethem, J.; Venstermans, C.; Salgado, R.; Voormolen, M.; Van Hecke, W. Magnetic Resonance Imaging of the Brain. In *Clinical MR Imaging*; Reimer, P., Parizel, P.M., Meaney, J.F.M., Stichnoth, F.A., Eds.; Springer: Berlin, Heidelberg, 2010; pp. 107–195. [CrossRef]
4. Llamas, M. Gadolinium-Based Contrast Agents. Available online: <https://www.drugwatch.com/gadolinium/> (accessed on 12 December 2023).
5. Fraum, T.J.; Ludwig, D.R.; Bashir, M.R.; Fowler, K.J. Gadolinium-based contrast agents: A comprehensive risk assessment. *J. Magn. Reson. Imaging* **2017**, *46*, 338–353. [CrossRef] [PubMed]
6. Wahsner, J.; Gale, E.M.; Rodríguez-Rodríguez, A.; Caravan, P. Chemistry of MRI Contrast Agents: Current Challenges and New Frontiers. *Chem. Rev.* **2019**, *119*, 957–1057. [CrossRef] [PubMed]
7. Cowper, S.E.; Robin, H.S.; Steinberg, S.M.; Su, L.D.; Gupta, S.; LeBoit, P.E. Scleromyxoedema-like cutaneous diseases in renal-dialysis patients. *Lancet* **2000**, *356*, 1000. [CrossRef] [PubMed]
8. George, S.J.; Webb, S.M.; Abraham, J.L.; Cramer, S.P. Synchrotron X-ray analyses demonstrate phosphate-bound gadolinium in skin in nephrogenic systemic fibrosis. *Br. J. Dermatol.* **2010**, *163*, 1077–1081. [CrossRef]
9. Perazella, M.A. Current Status of Gadolinium Toxicity in Patients with Kidney Disease. *Clin. J. Am. Soc. Nephrol.* **2009**, *4*, 461–469. [CrossRef]
10. Weller, A.; Barber, J.L.; Olsen, Ø.E. Gadolinium and nephrogenic systemic fibrosis: An update. *Pediatr. Nephrol.* **2014**, *29*, 1927–1937. [CrossRef]
11. Le Fur, M.; Caravan, P. The biological fate of gadolinium-based MRI contrast agents: A call to action for bioinorganic chemists. *Metallomics* **2019**, *11*, 240–254. [CrossRef]

12. Schieda, N.; Blaichman, J.I.; Costa, A.F.; Glikstein, R.; Hurrell, C.; James, M.; Jabehdar Maralani, P.; Shabana, W.; Tang, A.; Tsampalieros, A.; et al. Gadolinium-Based Contrast Agents in Kidney Disease: A Comprehensive Review and Clinical Practice Guideline Issued by the Canadian Association of Radiologists. *Can. J. Kidney Health Dis.* **2018**, *5*, 2054358118778573. [[CrossRef](#)]
13. Do, C.; DeAgüero, J.; Brearley, A.; Trejo, X.; Howard, T.; Escobar, G.P.; Wagner, B. Gadolinium-Based Contrast Agent Use, Their Safety, and Practice Evolution. *Kidney360* **2020**, *1*, 561–568. [[CrossRef](#)] [[PubMed](#)]
14. FDA. FDA Drug Safety Communication: FDA Warns that Gadolinium-Based Contrast Agents (GBCAs) Are Retained in the Body; Requires New Class Warnings. Available online: <https://www.fda.gov/drugs/drug-safety-and-availability/fda-drug-safety-communication-fda-warns-gadolinium-based-contrast-agents-gbcas-are-retained-body> (accessed on 12 December 2023).
15. Winter, M.B.; Klemm, P.J.; Phillips-Piro, C.M.; Raymond, K.N.; Marletta, M.A. Porphyrin-Substituted H-NOX Proteins as High-Relaxivity MRI Contrast Agents. *Inorg. Chem.* **2013**, *52*, 2277–2279. [[CrossRef](#)] [[PubMed](#)]
16. Young, I.R.; Clarke, G.J.; Bailes, D.R.; Pennock, J.M.; Doyle, F.H.; Bydder, G.M. Enhancement of Relaxation Rate with Paramagnetic Contrast Agents in Nmr Imaging. *J. Comput. Tomogr.* **1981**, *5*, 543–547. [[CrossRef](#)] [[PubMed](#)]
17. Tan, M.; Ye, Z.; Jeong, E.-K.; Wu, X.; Parker, D.L.; Lu, Z.-R. Synthesis and Evaluation of Nanoglobular Macrocyclic Mn(II) Chelate Conjugates as Non-Gadolinium(III) MRI Contrast Agents. *Bioconjugate Chem.* **2011**, *22*, 931–937. [[CrossRef](#)] [[PubMed](#)]
18. Gallez, B.; Baudalet, C.; Adline, J.; Geurts, M.; Delzenne, N. Accumulation of manganese in the brain of mice after intravenous injection of manganese-based contrast agents. *Chem. Res. Toxicol.* **1997**, *10*, 360–363. [[CrossRef](#)] [[PubMed](#)]
19. Shokouhimehr, M.; Soehnlén, E.S.; Hao, J.; Griswold, M.; Flask, C.; Fan, X.; Basilion, J.P.; Basu, S.; Huang, S.D. Dual purpose Prussian blue nanoparticles for cellular imaging and drug delivery: A new generation of T-1-weighted MRI contrast and small molecule delivery agents. *J. Mater. Chem.* **2010**, *20*, 5251–5259. [[CrossRef](#)]
20. Kandanaipitiye, M.S.; Valley, B.; Yang, L.D.; Fry, A.M.; Woodward, P.M.; Huang, S.D. Gallium Analogue of Soluble Prussian Blue $\text{K}_2\text{GaFe}(\text{CN})_6 \cdot n\text{H}_2\text{O}$: Synthesis, Characterization, and Potential Biomedical Applications. *Inorg. Chem.* **2013**, *52*, 2790–2792. [[CrossRef](#)] [[PubMed](#)]
21. World Health Organization. World Health Organization Model List of Essential Medicines: 21st List. Available online: <https://apps.who.int/iris/handle/10665/325771> (accessed on 12 December 2023).
22. Wang, H.; Huang, S.D.; Yan, L.; Hu, M.Y.; Zhao, J.; Alp, E.E.; Yoda, Y.; Petersen, C.M.; Thompson, M.K. Europium-151 and iron-57 nuclear resonant vibrational spectroscopy of naturally abundant $\text{K}_2\text{Eu}(\text{iii})\text{Fe}(\text{ii})(\text{CN})_6$ and $\text{Eu}(\text{iii})\text{Fe}(\text{iii})(\text{CN})_6$ complexes. *Dalton Trans.* **2022**, *51*, 17753–17761. [[CrossRef](#)]
23. Buser, H.J.; Schwarzenbach, D.; Petter, W.; Ludi, A. The crystal structure of Prussian Blue: $\text{Fe}_4[\text{Fe}(\text{CN})_6]_3 \cdot x\text{H}_2\text{O}$. *Inorg. Chem.* **1977**, *16*, 2704–2710. [[CrossRef](#)]
24. Zhang, J.; Deng, L.; Feng, M.; Zeng, L.; Hu, M.; Zhu, Y. Low-defect $\text{K}_2\text{Mn}[\text{Fe}(\text{CN})_6]$ -reduced graphene oxide composite for high-performance potassium-ion batteries. *Chem. Commun.* **2021**, *57*, 8632–8635. [[CrossRef](#)]
25. Shin, J.; Anisur, R.M.; Ko, M.K.; Im, G.H.; Lee, J.H.; Lee, I.S. Hollow Manganese Oxide Nanoparticles as Multifunctional Agents for Magnetic Resonance Imaging and Drug Delivery. *Angew. Chem. Int. Ed.* **2009**, *48*, 321–324. [[CrossRef](#)] [[PubMed](#)]
26. Wasinger, E.C.; de Groot, F.M.F.; Hedman, B.; Hodgson, K.O.; Solomon, E.I. L-edge X-ray Absorption Spectroscopy of Non-Heme Iron Sites: Experimental Determination of Differential Orbital Covalency. *J. Am. Chem. Soc.* **2003**, *125*, 12894–12906. [[CrossRef](#)] [[PubMed](#)]
27. Denny, Y.R.; Takahashi, K.; Niki, K.; Yang, D.S.; Fujikawa, T.; Kang, H.J. Ni K-edge XAFS analysis of NiO thin film with multiple scattering theory. *Surf. Interface Anal.* **2014**, *46*, 997–999. [[CrossRef](#)]
28. Wang, H.; Braun, A.; Cramer, S.P.; Gee, L.B.; Yoda, Y. Nuclear Resonance Vibrational Spectroscopy: A Modern Tool to Pinpoint Site-Specific Cooperative Processes. *Crystals* **2021**, *11*, 909. [[CrossRef](#)] [[PubMed](#)]
29. Cressey, G.; Henderson, C.M.B.; van der Laan, G. Use of L-edge X-ray absorption spectroscopy to characterize multiple valence states of 3d transition metals; a new probe for mineralogical and geochemical research. *Phys. Chem. Miner.* **1993**, *20*, 111–119. [[CrossRef](#)]
30. Baker, M.L.; Mara, M.W.; Yan, J.J.; Hodgson, K.O.; Hedman, B.; Solomon, E.I. K- and L-edge X-ray absorption spectroscopy (XAS) and resonant inelastic X-ray scattering (RIXS) determination of differential orbital covalency (DOC) of transition metal sites. *Coord. Chem. Rev.* **2017**, *345*, 182–208. [[CrossRef](#)] [[PubMed](#)]
31. Xi, L.; Schwanke, C.; Xiao, J.; Abdi, F.F.; Zaharieva, I.; Lange, K.M. In Situ L-Edge XAS Study of a Manganese Oxide Water Oxidation Catalyst. *J. Phys. Chem. C* **2017**, *121*, 12003–12009. [[CrossRef](#)]
32. Penner-Hahn, J.E.; Fronko, R.M.; Pecoraro, V.L.; Yocum, C.F.; Betts, S.D.; Bowlby, N.R. Structural Characterization of the Manganese Sites in the Photosynthetic Oxygen-Evolving Complex Using X-Ray Absorption Spectroscopy. *J. Am. Chem. Soc.* **1990**, *112*, 2549–2557. [[CrossRef](#)]
33. Westre, T.E.; Kennepohl, P.; DeWitt, J.G.; Hedman, B.; Hodgson, K.O.; Solomon, E.I. A multiplet analysis of Fe K-edge 1s- \rightarrow 3d pre-edge features of iron complexes. *J. Am. Chem. Soc.* **1997**, *119*, 6297–6314. [[CrossRef](#)]
34. Penner-Hahn, J.E. X-ray Absorption Spectroscopy. In *eLS*; Wiley Online Library: Hoboken, NJ, USA, 2005. [[CrossRef](#)]
35. Stöhr, J. *NEXAFS Spectroscopy*; Springer: New York, NY, USA, 2003.
36. Wang, H.; Friedrich, S.; Li, L.; Mao, Z.; Ge, P.; Balasubramanian, M.; Patil, D.S. L-edge sum rule analysis on 3d transition metal sites: From d10 to d0 and towards application to extremely dilute metallo-enzymes. *Phys. Chem. Chem. Phys.* **2018**, *20*, 8166–8176. [[CrossRef](#)]

37. de Groot, F. High resolution X-ray emission and X-ray absorption spectroscopy. *Chem. Rev.* **2001**, *101*, 1779–1808. [[CrossRef](#)] [[PubMed](#)]
38. Wang, H.X.; Ralston, C.Y.; Patil, D.S.; Jones, R.M.; Gu, W.; Verhagen, M.; Adams, M.; Ge, P.; Riordan, C.; Marganian, C.A.; et al. Nickel L-edge soft X-ray spectroscopy of nickel-iron hydrogenases and model compounds—Evidence for high-spin nickel(II) in the active enzyme. *J. Am. Chem. Soc.* **2000**, *122*, 10544–10552. [[CrossRef](#)]
39. Nakamura, T.; Oike, R.; Kimura, Y.; Tamenori, Y.; Kawada, T.; Amezawa, K. Operando Soft X-ray Absorption Spectroscopic Study on a Solid Oxide Fuel Cell Cathode during Electrochemical Oxygen Reduction. *ChemSusChem* **2017**, *10*, 2008–2014. [[CrossRef](#)] [[PubMed](#)]
40. Kuiper, P.; Guo, J.H.; Sàthe, C.; Duda, L.C.; Nordgren, J.; Pothuizen, J.J.M.; de Groot, F.M.F.; Sawatzky, G.A. Resonant X-Ray Raman Spectra of Cu *dd* Excitations in Sr₂CuO₂Cl₂. *Phys. Rev. Lett.* **1998**, *80*, 5204–5207. [[CrossRef](#)]
41. Freelon, B.; Augustsson, A.; Guo, J.H.; Medaglia, P.G.; Tebano, A.; Balestrino, G. Electron correlation and charge transfer in superconducting superlattices. *Phys. Rev. Lett.* **2006**, *96*, 017003. [[CrossRef](#)] [[PubMed](#)]
42. Kapilashrami, M.; Zhang, Y.; Liu, Y.-S.; Hagfeldt, A.; Guo, J. Probing the Optical Property and Electronic Structure of TiO₂ Nanomaterials for Renewable Energy Applications. *Chem. Rev.* **2014**, *114*, 9662–9707. [[CrossRef](#)] [[PubMed](#)]
43. Jang, J.-W.; Du, C.; Ye, Y.; Lin, Y.; Yao, X.; Thorne, J.; Liu, E.; McMahon, G.; Zhu, J.; Javey, A.; et al. Enabling unassisted solar water splitting by iron oxide and silicon. *Nat. Commun.* **2015**, *6*, 7447. [[CrossRef](#)]
44. Chumakov, A.I.; Ruffer, R.; Leupold, O.; Sergueev, I. Insight to Dynamics of Molecules with Nuclear Inelastic Scattering. *Struct. Chem.* **2003**, *14*, 109–119. [[CrossRef](#)]
45. Lehnert, N.; Sage, J.T.; Silvernail, N.; Scheidt, W.R.; Alp, E.E.; Sturhahn, W.; Zhao, J. Oriented Single-Crystal Nuclear Resonance Vibrational Spectroscopy of [Fe(TPP)(MI)(NO)]: Quantitative Assessment of the trans Effect of NO. *Inorg. Chem.* **2010**, *49*, 7197–7215. [[CrossRef](#)]
46. Zhao, J.; Sturhahn, W.; Lin, J.-F.; Shen, G.; Apl, E.; Mao, H.-K. Nuclear resonant scattering at high pressure and high temperature. *High Press. Res. Int. J.* **2004**, *24*, 447–457. [[CrossRef](#)]
47. Chumakov, A.I.; Ruffer, R.; Grünsteudel, H.; Grünsteudel, H.F.; Grübel, G.; Metge, J.; Leupold, O.; Goodwin, H.A. Energy Dependence of Nuclear Recoil Measured with Incoherent Nuclear Scattering of Synchrotron Radiation. *EPL Europhys. Lett.* **1995**, *30*, 427. [[CrossRef](#)]
48. Ogata, H.; Kramer, T.; Wang, H.; Schilter, D.; Pelmeshnikov, V.; van Gastel, M.; Neese, F.; Rauchfuss, T.B.; Gee, L.B.; Scott, A.D.; et al. Hydride bridge in [NiFe]-hydrogenase observed by nuclear resonance vibrational spectroscopy. *Nat. Commun.* **2015**, *6*, 7890. [[CrossRef](#)] [[PubMed](#)]
49. Guo, Y.; Wang, H.; Xiao, Y.; Vogt, S.; Thauer, R.K.; Shima, S.; Volkens, P.I.; Rauchfuss, T.B.; Pelmeshnikov, V.; Case, D.A.; et al. Characterization of the Fe site in iron-sulfur cluster-free hydrogenase (Hmd) and of a model compound via nuclear resonance vibrational spectroscopy (NRVS). *Inorg. Chem.* **2008**, *47*, 3969–3977. [[CrossRef](#)] [[PubMed](#)]
50. Petit, S.; Madejova, J. Chapter 2.7—Fourier Transform Infrared Spectroscopy. In *Developments in Clay Science*; Bergaya, F., Lagaly, G., Eds.; Elsevier: Amsterdam, The Netherlands, 2013; Volume 5, pp. 213–231.
51. Scheidt, W.R.; Li, J.; Sage, J.T. What Can Be Learned from Nuclear Resonance Vibrational Spectroscopy: Vibrational Dynamics and Hemes. *Chem. Rev.* **2017**, *117*, 12532–12563. [[CrossRef](#)] [[PubMed](#)]
52. Wang, J.; Li, L.; Wang, H. Machine learning concept in de-spiking process for nuclear resonant vibrational spectra—Automation using no external parameter. *Vib. Spectrosc.* **2022**, *119*, 103352. [[CrossRef](#)]
53. Sturhahn, W. CONUSS and PHOENIX: Evaluation of nuclear resonant scattering data. *Hyperfine Interact.* **2000**, *125*, 149–172. [[CrossRef](#)]
54. Wang, H.; Salzberg, A.P.; Weiner, B.R. Laser ablation of aluminum at 193, 248, and 351 nm. *Appl. Phys. Lett.* **1991**, *59*, 935–937. [[CrossRef](#)]
55. Barnhard, K.I.; He, M.; Weiner, B.R. Excited-State Dynamics of CH₂CHO ($\tilde{B}2A''$). *J. Phys. Chem.* **1996**, *100*, 2784–2790. [[CrossRef](#)]
56. Wu, F.; Chen, X.; Weiner, B.R. The Photochemistry of Ethylene Episulfoxide. *J. Am. Chem. Soc.* **1996**, *118*, 8417–8424. [[CrossRef](#)]
57. Murai, N.; Fukuda, T.; Nakajima, M.; Kawamura, M.; Ishikawa, D.; Tajima, S.; Baron, A.Q.R. Lattice dynamics in FeSe via inelastic x-ray scattering and first-principles calculations. *Phys. Rev. B* **2020**, *101*, 035126. [[CrossRef](#)]
58. Chumakov, A.I.; Metge, J.; Baron, A.Q.R.; Grünsteudel, H.; Grünsteudel, H.F.; Ruffer, R.; Ishikawa, T. An X-ray monochromator with 1.65 meV energy resolution. *Nucl. Instrum. Methods Phys. Res. Sect. A Accel. Spectrometers Detect. Assoc. Equip.* **1996**, *383*, 642–644. [[CrossRef](#)]
59. Toellner, T.S.; Alatas, A.; Said, A.; Shu, D.; Sturhahn, W.; Zhao, J. A cryogenically stabilized meV-monochromator for hard X-rays. *J. Synchrotron Radiat.* **2006**, *13*, 211–215. [[CrossRef](#)] [[PubMed](#)]
60. Kandanapitiye, M.S.; Dassanayake, T.M.; Dassanayake, A.C.; Shelestak, J.; Clements, R.J.; Fernando, C.; Huang, S.D. K₂Mn₃[FeII(CN)₆]₂ NPs with High T₁-Relaxivity Attributable to Water Coordination on the Mn(II) Center for Gastrointestinal Tract MR Imaging. *Adv. Healthc. Mater.* **2021**, *10*, 2100987. [[CrossRef](#)] [[PubMed](#)]
61. Albracht, S.P.J. Nickel Hydrogenases—In Search Of the Active Site. *Biochim. Biophys. Acta-Bioenerg.* **1994**, *1188*, 167–204. [[CrossRef](#)] [[PubMed](#)]
62. Bertini, I.; Gray, H.B.; Lippard, S.J.; Valentine, J.S. *Bioinorganic Chemistry*; University Science Books: Mill Valley, CA, USA, 1994.
63. Cammack, R.; Fernandez, V.M.; Hatchikian, E.C. Nickel-iron Hydrogenases. In *Inorganic Microbial Sulfur Metabolism*; LeGall, J., Peck, H.D., Jr., Eds.; Academic Press Inc.: San Diego, CA, USA, 1994; Volume 243, pp. 43–67.

64. Pickering, I.J.; George, G.N.; Lewandowski, J.T.; Jacobson, A.J. Nickel K-Edge X-Ray Absorption Fine Structure of Lithium Nickel Oxides. *J. Am. Chem. Soc.* **1993**, *115*, 4137–4144. [[CrossRef](#)]
65. Coyle, C.L.; Stiefel, E.I. The Coordination Chemistry of Nickel: An Introductory Survey. In *The Bioinorganic Chemistry of Nickel*; Lancaster, J.R., Jr., Ed.; VCH Publishers: New York, NY, USA, 1988; pp. 1–28.
66. Lee, J.; Kitchaev, D.A.; Kwon, D.-H.; Lee, C.-W.; Papp, J.K.; Liu, Y.-S.; Lun, Z.; Clément, R.J.; Shi, T.; McCloskey, B.D.; et al. Reversible Mn²⁺/Mn⁴⁺ double redox in lithium-excess cathode materials. *Nature* **2018**, *556*, 185–190. [[CrossRef](#)] [[PubMed](#)]
67. Gilbert, B.; Frazer, B.H.; Belz, A.; Conrad, P.G.; Nealon, K.H.; Haskel, D.; Lang, J.C.; Srajer, G.; De Stasio, G. Multiple Scattering Calculations of Bonding and X-ray Absorption Spectroscopy of Manganese Oxides. *J. Phys. Chem. A* **2003**, *107*, 2839–2847. [[CrossRef](#)]
68. Kubobuchi, K.; Mogi, M.; Ikeno, H.; Tanaka, I.; Imai, H.; Mizoguchi, T. Mn L_{2,3}-edge X-ray absorption spectroscopic studies on charge-discharge mechanism of Li₂MnO₃. *Appl. Phys. Lett.* **2014**, *104*, 053906. [[CrossRef](#)]
69. Jeong, S.; Milner, P.J.; Wan, L.F.; Liu, Y.-S.; Oktawiec, J.; Zaia, E.W.; Forse, A.C.; Leick, N.; Gennett, T.; Guo, J.; et al. Runaway Carbon Dioxide Conversion Leads to Enhanced Uptake in a Nanohybrid Form of Porous Magnesium Borohydride. *Adv. Mater.* **2019**, *31*, 1904252. [[CrossRef](#)]
70. Cramer, S.P.; Ma, Y.; Chen, C.; Sette, F.; Kipke, C.A.; Eichhorn, D.M.; Chan, M.K.; Armstrong, W.H.; Libby, I.E.; Christou, G.; et al. Ligand Field Strengths and Oxidation States from Manganese L-Edge Spectroscopy. *J. Am. Chem. Soc.* **1991**, *113*, 7937–7940. [[CrossRef](#)]
71. Grush, M.M.; Chen, J.; Stemmler, T.L.; George, S.J.; Ralston, C.Y.; Stibrany, R.T.; Gelasco, A.; Christou, G.; Gorun, S.M.; Penner-Hahn, J.E.; et al. Manganese L-Edge X-ray Absorption Spectroscopy of Manganese Catalase from *Lactobacillus plantarum* and Mixed Valence Manganese Complexes. *J. Am. Chem. Soc.* **1996**, *118*, 65–69. [[CrossRef](#)]
72. Kubin, M.; Guo, M.; Kroll, T.; Löchel, H.; Källman, E.; Baker, M.L.; Mitzner, R.; Gul, S.; Kern, J.; Föhlisch, A.; et al. Probing the oxidation state of transition metal complexes: A case study on how charge and spin densities determine Mn L-edge X-ray absorption energies. *Chem. Sci.* **2018**, *9*, 6813–6829. [[CrossRef](#)] [[PubMed](#)]
73. Lee, E.; Kim, D.H.; Hwang, J.; Kang, J.S.; Van Minh, N.; Yang, I.-S.; Ueno, T.; Sawada, M. Soft x-ray absorption spectroscopy study of Prussian blue analogue ACo[Fe(CN)₆]H₂O nano-particles (A=Na, K). *J. Korean Phys. Soc.* **2013**, *62*, 1910–1913. [[CrossRef](#)]
74. Lalithambika, S.S.N.; Atak, K.; Seidel, R.; Neubauer, A.; Brandenburg, T.; Xiao, J.; Winter, B.; Aziz, E.F. Chemical bonding in aqueous hexacyano cobaltate from photon- and electron-detection perspectives. *Sci. Rep.* **2017**, *7*, 40811. [[CrossRef](#)] [[PubMed](#)]
75. Chang, C.F.; Hu, Z.; Wu, H.; Burnus, T.; Hollmann, N.; Benomar, M.; Lorenz, T.; Tanaka, A.; Lin, H.J.; Hsieh, H.H.; et al. Spin Blockade, Orbital Occupation, and Charge Ordering in La_{1.5}Sr_{0.5}CoO₄. *Phys. Rev. Lett.* **2009**, *102*, 116401. [[CrossRef](#)] [[PubMed](#)]
76. Istomin, S.Y.; Tyablikov, O.A.; Kazakov, S.M.; Antipov, E.V.; Kurbakov, A.I.; Tsirlin, A.A.; Hollmann, N.; Chin, Y.Y.; Lin, H.J.; Chen, C.T.; et al. An unusual high-spin ground state of Co³⁺ in octahedral coordination in brownmillerite-type cobalt oxide. *Dalton Trans.* **2015**, *44*, 10708–10713. [[CrossRef](#)]
77. Miedema, P.S.; van Schooneveld, M.M.; Bogerd, R.; Rocha, T.C.R.; Hävecker, M.; Knop-Gericke, A.; de Groot, F.M.F. Oxygen Binding to Cobalt and Iron Phthalocyanines As Determined from in Situ X-ray Absorption Spectroscopy. *J. Phys. Chem. C* **2011**, *115*, 25422–25428. [[CrossRef](#)]
78. Hocking, R.K.; Wasinger, E.C.; de Groot, F.M.F.; Hodgson, K.O.; Hedman, B.; Solomon, E.I. Fe L-Edge XAS Studies of K₄[Fe(CN)₆] and K₃[Fe(CN)₆]: A Direct Probe of Back-Bonding. *J. Am. Chem. Soc.* **2006**, *128*, 10442–10451. [[CrossRef](#)]
79. George, S.J.; Fu, J.; Guo, Y.; Drury, O.B.; Friedrich, S.; Rauchfuss, T.; Volkers, P.I.; Peters, J.C.; Scott, V.; Brown, S.D.; et al. X-ray photochemistry in iron complexes from Fe(0) to Fe(IV)—Can a bug become a feature? *Inorganica Chim. Acta* **2008**, *361*, 1157–1165. [[CrossRef](#)]
80. Weber, B. *Coordination Chemistry—Basics and Current Trends*; Springer: Berlin/Heidelberg, Germany, 2023. [[CrossRef](#)]
81. Pike, R.D. Structure and Bonding in Copper(I) Carbonyl and Cyanide Complexes. *Organometallics* **2012**, *31*, 7647–7660. [[CrossRef](#)]
82. Frenking, G.; Fernández, I.; Holzmann, N.; Pan, S.; Krossing, I.; Zhou, M. Metal–CO Bonding in Mononuclear Transition Metal Carbonyl Complexes. *JACS Au* **2021**, *1*, 623–645. [[CrossRef](#)] [[PubMed](#)]
83. Everett, J.; Céspedes, E.; Shelford, L.R.; Exley, C.; Collingwood, J.F.; Dobson, J.; van der Laan, G.; Jenkins, C.A.; Arenholz, E.; Telling, N.D. Ferrous iron formation following the co-aggregation of ferric iron and the Alzheimer’s disease peptide β-amyloid (1–42). *J. R. Soc. Interface* **2014**, *11*, 20140165. [[CrossRef](#)] [[PubMed](#)]
84. Miedema, P.S.; de Groot, F.M.F. The iron L edges: Fe 2p X-ray absorption and electron energy loss spectroscopy. *J. Electron Spectrosc. Relat. Phenom.* **2013**, *187*, 32–48. [[CrossRef](#)]
85. Bhattacharyya, A.; Stavitski, E.; Dvorak, J.; Martínez, C.E. Redox interactions between Fe and cysteine: Spectroscopic studies and multiplet calculations. *Geochim. Cosmochim. Acta* **2013**, *122*, 89–100. [[CrossRef](#)]
86. Collison, D.; Garner, C.D.; McGrath, C.M.; Mosselmans, J.F.W.; Roper, M.D.; Seddon, J.M.W.; Sinn, E.; Young, N.A. Soft X-ray photochemistry at the L_{2,3}-edges in K₃[Fe(CN)₆], [Co(acac)₃] and [Cp₂Fe][BF₃]. *J. Synchrotron Radiat.* **1999**, *6*, 585–587. [[CrossRef](#)] [[PubMed](#)]
87. van Schooneveld, M.M.; DeBeer, S. A close look at dose: Toward L-edge XAS spectral uniformity, dose quantification and prediction of metal ion photoreduction. *J. Electron Spectrosc. Relat. Phenom.* **2015**, *198*, 31–56. [[CrossRef](#)]

-
88. Parasar, D.; Jayaratna, N.B.; Muñoz-Castro, A.; Conway, A.E.; Mykhailiuk, P.K.; Dias, H.V.R. Carbonyl complexes of copper(I) stabilized by bridging fluorinated pyrazolates and halide ions. *Dalton Trans.* **2019**, *48*, 6358–6371. [[CrossRef](#)]
89. Eaton, J.P.; Nicholls, D. The complex cyanides of chromium(II) and chromium(0). *Transit. Met. Chem.* **1981**, *6*, 203–206. [[CrossRef](#)]

Disclaimer/Publisher's Note: The statements, opinions and data contained in all publications are solely those of the individual author(s) and contributor(s) and not of MDPI and/or the editor(s). MDPI and/or the editor(s) disclaim responsibility for any injury to people or property resulting from any ideas, methods, instructions or products referred to in the content.